

Three-Dimensional Inversion of Magnetotelluric Data in Study of Focal Zones of Earthquakes in the South of the Altai–Sayan Region

V.V. Belyavsky✉

Schmidt Institute of Physics of the Earth, Russian Academy of Sciences, Geoelectromagnetic Research Centre,
Troitsk, Moscow, 142190, Russia

Received 9 April 2018; received in revised form 26 December 2018; accepted 21 March 2019

Abstract—The potentialities of the 3D inversion program WSINV3DMT were estimated on the model $[Z_m]$ and observed $[Z_{ob}]$ components of the impedance tensor and its invariants during the construction of geoelectrical models for the southern part of the Altai–Sayan region characterized by a three-dimensional distribution of electrical conductivity. These components were obtained for a 3D model constructed by the method of interactive selection of the 3D model induction curves for the experimental ones. Testing of the WSINV3DMT program on the model magnetotelluric data showed the possibility of not only isolation of blocks of high electrical conductivity but also of the appearance of conductivity anomalies different from the model ones. The paper presents a 3D geoelectrical model for the southern focal zones of the region, constructed with the use of the WSINV3DMT program and the proposed method of interpretation. The isolated blocks of low electrical resistivity are correlated with the location of earthquake foci, deep faults, and regions of high absorption of earthquake exchange waves.

Keywords: magnetotelluric sounding, 3D inversion, electrical resistivity, focal zones of earthquakes

INTRODUCTION

The interest in distribution of geoelectric parameters in the lithosphere is caused by the dependence of electrical resistivity on the degree of fluid mineralization, adhesion, and liquid fraction saturation of rocks. Resistivity distribution in the crust makes it possible to identify the most fluid-weakened and saturated zones, along which crustal blocks are displaced and whose pinchout portions have the highest concentration of areas with maximum stresses (Rice, 1982), where seismic events often occur.

Kissin (2009) showed that seismic activity is most often manifested at the interfaces of structures with contrasting geoelectric parameters, high horizontal seismic velocity gradients or different S-wave absorption parameters. The latter depend, among other things, on fluid saturation, which in turn is linked to metamorphic dehydration processes. According to the fluid-metamorphogenic model (Rodkin and Rundquist, 2017), seismic processes stem from tectonic stresses and metamorphic processes, while changes in permeability and porosity of the medium depend on adhesion of the fluid-pore space and pore sizes. Since pores may be filled by fluids, and water is the main component of the fluid system (Kissin, 2009), they may be considered the components of the ‘intracrustal hydrosphere’.

Deep magnetotelluric (MT) research is topical because the studied area of the Altai–Sayan region is characterized by seismic shock intensities up to 8–9 (Fig. 1, inset). It is shown how geoelectric parameters of deep faults and conductive crustal blocks may be estimated using 3D inversion of experimental MT sounding (MTS) curves. Their link with earthquake foci and zones with increased absorption of converted seismic waves of earthquakes is demonstrated.

3D inversion experiments performed using WSINV3DMT software (Siripunvaraporn et al., 2005) for model-based impedance matrices $[Z_m]$ showed that, if the studied profile intersects blocks with different resistivity values, then the procedure is capable of recovering their positions, given the adequate starting model (Ivanov and Pushkarev, 2012). If MTS profile deviates by 45° from the direction of the stretched 3D block (Kiyan et al., 2014), then its position is also recovered by inversion of all or main values of impedance matrices for impedances directed along its faces.

In the presented study, we investigated two intersecting orthogonal MTS profiles, which, given the available data on resistivity distribution in the upper part of the section (Dobretsov et al., 2016; Belyavsky, 2017), allows us to presume a match between deep geoelectric sections and the results of 3D inversion of MTS curves.

Activation of the Altai–Sayan folded area is associated with regional compression arising from the collision of the Indostan plate with the Eurasian continent. Development of its Cenozoic structure “is a result of domino-like long-dis-

✉ Corresponding author.

E-mail address: victor.belyavsky@list.ru (V.V. Belyavsky)

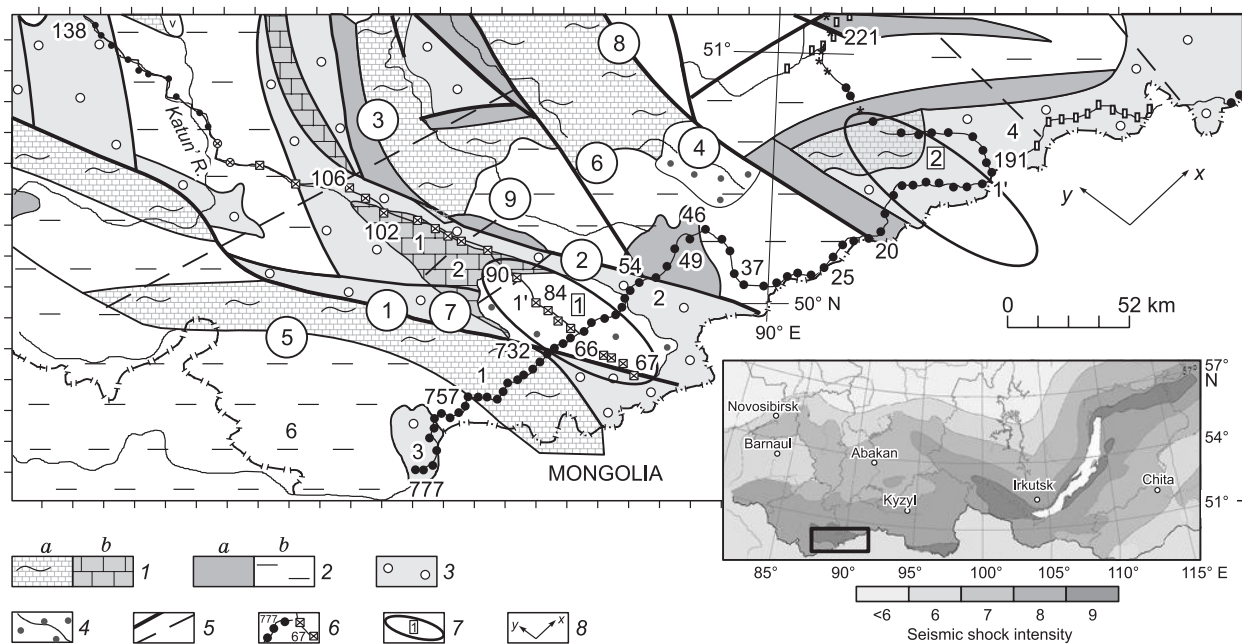


Fig. 1. Locations of MTS profiles on the structural-geological regionalization scheme of the Altai–Sayan region (Matrosov et al., 1988). 1, Tectonostratigraphic areas (TSAs) of late proterozooids: *a*, greenschist Baikhalide escarpments (1, South Chuya); *b*, terrigenous-siliceous-carbonate formation covers (2, Chagan-Uzun block); 2, Caledonide TSAs: *a*, early Caledonian subductional complexes with ophiolite associations; *b*, late Caledonian passive continental margins (6, South Kholzun); 3, orogenic-stage Caledonide TSAs (2, Yustyd; 3, Kalguta; 4, Tuva); 4, postorogenic activated TSAs (1, 1', Kurai and Chuya basins); 5, deep faults (digits in circles): 1, Bashelan; 2, Kurai; 3, Teletskoe; 4, East Shapshal; 5, South Terekta; 6, Chulyshman; 7, Central Chuya; 8, Shapshal; 9, RS (fault in accordance with earthquake converted wave data), dashed lines indicate hidden faults; 6, MTS sites along the Ukok–Sagly (777–1), Biisk–Tashanta (67–138), and Sagly–Shira (191–221) profiles; 7, earthquake epicenter zones (digits in squares) (1, Altai, 2, Ureg Nuur); 8, directions of *X* and *Y* axes in 3D models.

tance transmission of deformations from the Indo-Eurasian collision through stiff structures of Precambrian microcontinents located in the midst of Paleozoic–Mesozoic folded areas” (Buslov et al., 2013, p. 1623). The same authors have also demonstrated that a number of tectonic elements involved in the formation of late Paleozoic orogenic structures were accompanied by high-amplitude strike-slips and thrusts with different orientations.

The present stage of neotectonic activity manifests itself in the intensification of vertical movements in the areas of uplifts and basins, as well as NNW-oriented compression, which primarily affects positive structures of Gorny Altai (Matrosov et al., 1988; Rebetsky et al., 2013). Evolution of the concepts regarding formation of folded structures of Gorny Altai taking into account its collisional nature was achieved via calculations of stress tensors for the studied fault system. They made it possible to assume that creep movement of stiff crustal blocks along the semi-molten mantle, as well as the mantle itself, away from the low-velocity seismic mantle dome, could be the primary driving force of tectonic activity (Kuznetsova et al., 1999). This process was accompanied by penetration of semimolten mantle diapirs into the crust that later formed the structure of the upper crust. Calculations of stress tensors also demonstrate that the erosion and denudation leading to horizontal compressions within uplifts and extensions below the inter-

mountain troughs have to be taken into account. Rebetsky et al. (2013) emphasize the observed dependence of the present stress state of the crust on deep crustal and mantle non-uniformities.

The zone of interest is located within the Caledonides of the West Sayan region, i.e., Kurai, Chuya, and Uvs Nuur basins filled with Cenozoic molassoid, including coal-bearing, sediments (Fig. 1). The studied area is bounded in the west by the South Terekta and Bashelan faults, in the east—by the Shapshal fault, and in the north—by the Kurai fault. Strike-slips and upthrow-strike-slip faults got formed along their NW fragments, and late Cenozoic thrusts—along their near E–W and NE branches and lower-rank faults (Dobretsov et al., 2016).

BRIEF DESCRIPTION OF SOUTHERN FOCAL ZONES OF EARTHQUAKES IN THE ALTAI–SAYAN REGION

The Altai and Shapshal focal zones of earthquakes are identified in the studied area. NW-directed epicenter field of the Altai (sized 150×100 km) is located within the Kurai and Chuya basins and Chagan-Uzun horst that separates them. It is confined within the intersection area of the activated deep faults with different orientations (Fig. 1), namely Kurai, Bashelan, South Terekta, Central Chuya, and RS.

The hypocenter of the Altai earthquake (September 27, 2003) is located at the depth of 8.8 km with $M = 7.3$ below the western part of the Chagan-Uzun block. It is associated with decreased P-wave velocity zone at the depths of 5–10 km with V_p varying from 6.35 to 6.20 km/s below the NW edge of the Chuya basin (Liseikin and Soloviev, 2005). Aftershock hypocenters of the Altai earthquake located at depths of 2–20 km spread below the NW edges of the Chuya and Kurai basins and in the vicinity of the Central Chuya and RS faults. Zones with increased absorption of P- and S- converted waves ($K > 0.0009$ dB/km) and lateral decrease in their velocities in the upper crust are identified here as well (Belyavsky and Rakitov, 2012).

Epicenter field of the Shapshal focal zone sized 120×45 km (Fig. 1) is located at the interface of two contrasting neotectonic blocks, namely the subsiding (E–W-directed) western edge of the Uvs Nuur basin and the rising block structures of the Tuva folded system with NW strike direction. Ruptures occur in the focal area in the Shapshal fault zone with near N–S directed blocks with widths up to 15 km and lengths of 60–120 km.

Orientation of the epicenter field of the Shapshal focus is defined by its confinement to the active Shapshal fault zone representing the interface between the blocks that move vertically in opposite directions. In 1970–2007, earthquake hypocenters in the Uureg Nuur earthquake area were located at the depths from 3 to 23 km with maxima at 6–8 and 12 km, while the aftershock process was confined within intrablock faults (Emanov et al., 2012). The epicenter of the Uureg Nuur earthquake with $M = 7.0$ (May 15, 1970) was located at the depth of 12 km, where a strong velocity layering is no longer present in the crust, and the blocks with enhanced attenuation of earthquake converted waves ($K > 0.0009$ dB/km) were identified to the north, which extended to the depths $H = 40$ –50 km (Belyavsky and Rakitov, 2012).

Vertical displacements along the major fault zones near focal areas did not exceed 3–4 km, while horizontal shifts along the NW-directed faults reached 20–40 km. The area of mobile zones increased via crushing of the edge fragments of stable rim blocks and their engagement in upward movement (Novikov, 2004).

CONSTRUCTION OF GEOELECTRIC MODELS OF THE ALTAI AND SHAPSHAL FOCAL ZONES OF EARTHQUAKES

The considered area of the Altai–Sayan region is represented by combination of isometric blocks of various ages (Novikov, 2004). The faults that separate the blocks are characterized by different orientations, and structural lines of the region are superimposed by isometric molassoid basins of the Cenozoic age. Distribution of phase-sensitive asymmetry of impedance matrices is another indication of a 3D structure of focal zones of earthquakes (Belyavsky,

2017). Sedimentary covers of basins and the upper parts of their edges were considered as the upper level of the geoelectric model. The parameters of the underlying lower level were determined during 3D inversion of MT data.

Previously, geoelectric models of the lithosphere in the southern part of the Altai–Sayan region had been constructed by interactive selection of 3D model curves to match the experimental MTS curves (Belyavsky, 2017). The model curves were calculated based on 3D numerical modeling of MT fields using the Maxwell algorithm (Druskin and Knizhnerman, 1988). The calculation was performed within the period range $0.002 < T < 400$ s by the finite-difference method using the spectral approximation scheme based on eigenvalues of matrices from the system of equations derived from the Lanczos algorithm. Up to 100,000 Lanczos iterations were performed on the $130 \cdot 140 \cdot 70$ (X, Y, Z) mesh with a starting iteration from 3 km in the central blocks of the model to 20 km and above on the outside. Components of the impedance matrix $[Z_m]$, their invariants and orientations, asymmetry parameters, and 1D inversions for various impedance types were calculated using the service program (Belyavsky, 2017).

In addition to the 3D inversion of components of impedance matrices $[Z_m]$ and $[Z_{ob}]$, the possibility of using their invariants $|Z_{ob}^{maxH}|$, $|Z_{ob}^{minH}|$ and $|Z_m^{maxH}|$, $|Z_m^{minH}|$ had been considered as well (Council et al., 1986). This would reduce the number of impedance tensor components to be inverted from four to two, which would, in turn, simplify the comparison of the initial and model data and reduce the machine time needed for MTS inversion.

The 3D model of the southern part of Altai–Sayan region (Fig. 2) constructed using the Maxwell algorithm based on matching 3D model-based impedances of maximum and minimum induction $|Z_m^{maxH}|$, $|Z_m^{minH}|$ (Council et al., 1986) and the experimental $|Z_{ob}^{maxH}|$ and $|Z_{ob}^{minH}|$ values with a 10–20% average mean square relative error and agreeing with the hypothesis that fluid is generated in the mantle was accepted as a test model. The model was constructed as follows:

- a primary geoelectric model of the upper level and fault locations was developed in accordance with 1D inversion of maximum Z_{ob}^{maxH} and minimum Z_{ob}^{minH} induction curves;
- experimental $|Z_{ob}^{maxH}|$ and $|Z_{ob}^{minH}|$ values were normalized to reduce the shift effect in MTS curves before performing their 1D inversion;
- geoelectric models were constructed by fitting 3D model-based $|Z_m^{maxH}|$ and $|Z_m^{minH}|$ values calculated for the adjusted primary model to $|Z_{ob}^{maxH}|$ and $|Z_{ob}^{minH}|$ impedance values.

The final stage of constructing the 3D model of focal zones was to apply the 3D inversion software WSINV3D-MT (Siripunvaraporn et al., 2005) to impedance matrix components $[Z_{ob}]$ and Z_{ob}^{maxH} , Z_{ob}^{minH} as follows:

- WSINV3DMT software was adjusted to the test model of the Altai–Sayan region (Figs. 2, 3) for matrices $[Z_m]$ and

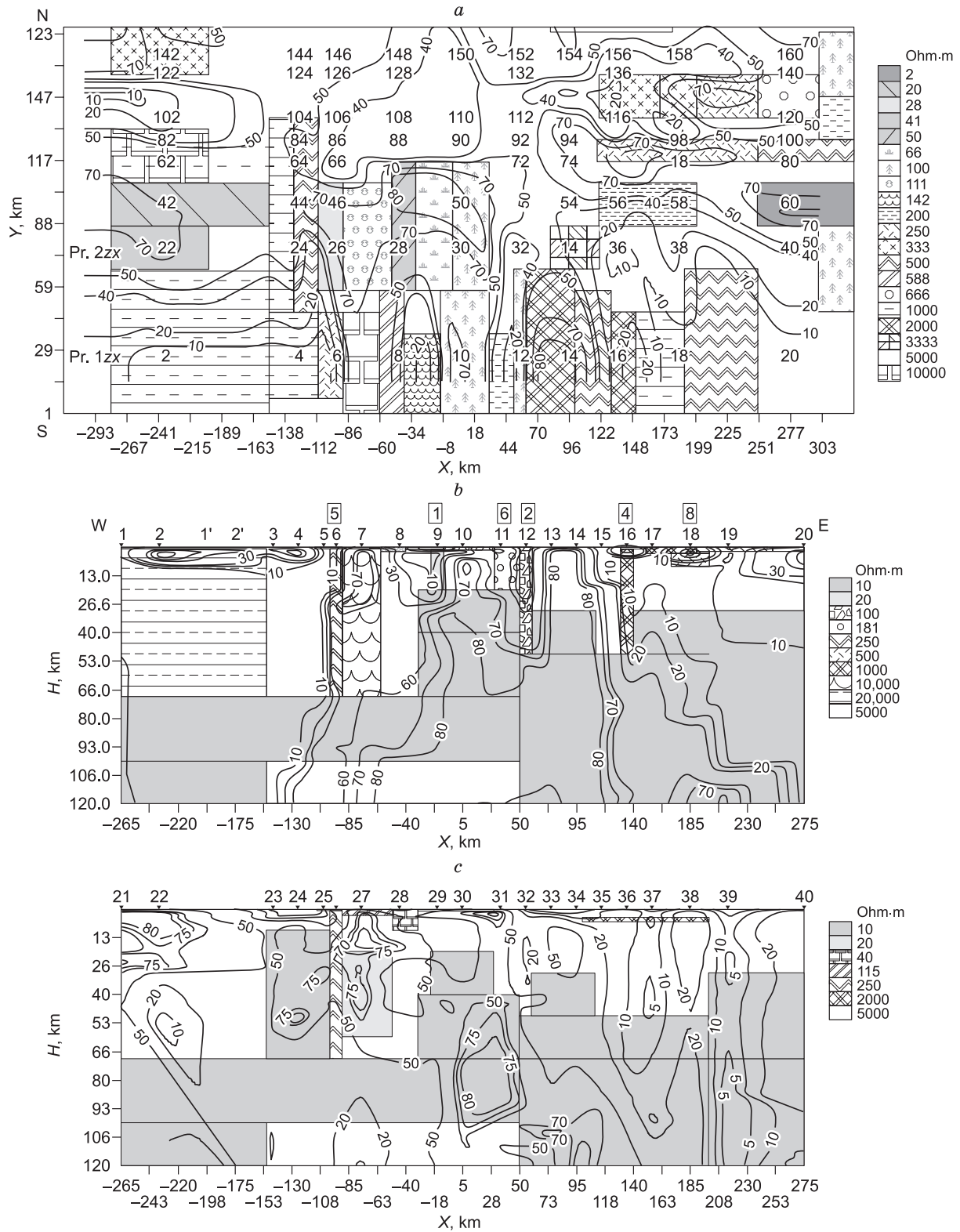


Fig. 2. Sections of the 3D test model (Belyavsky, 2017): *a*, directions of magnetic field angles θ_H^1 for unit magnetic vectors are presented for $Z = 0$ km at the impedance of maximum induction for $Z_m^{\max H}$ with period $T = 27$ s; *b*, *c* are the sections along Profiles 1zx and 2zx. Isolines represent θ_H^1 angles as a function of penetration depth of the MT field. Digits on models indicate numbers of OPs of MT fields. Numbers of deep faults (Fig. 1) are shown in squares. ER scale is shown on the right.

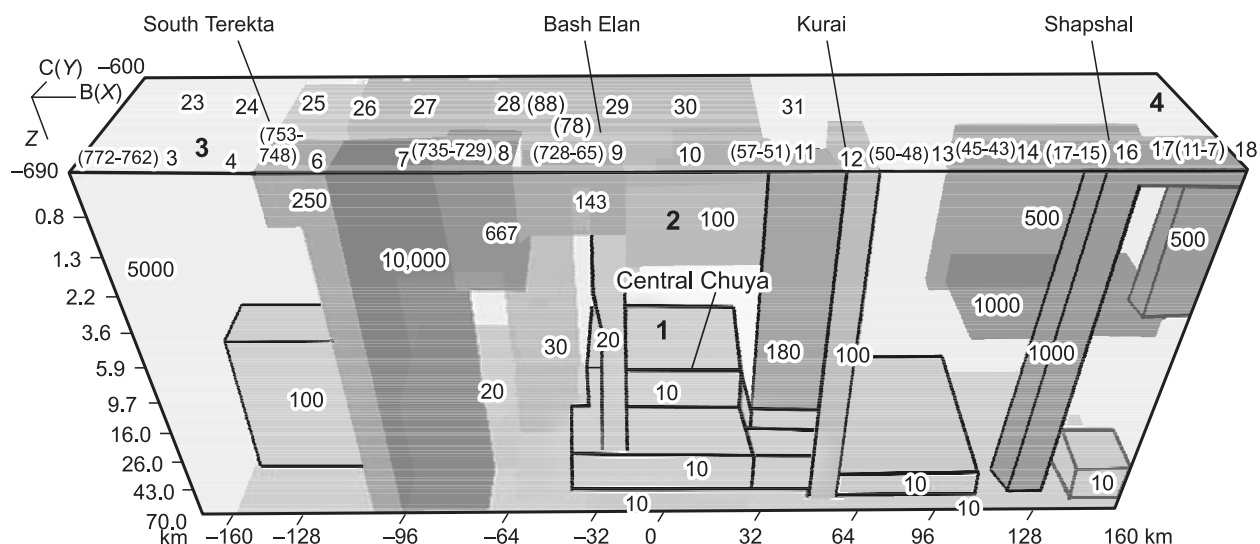


Fig. 3. A view of a simplified geoelectric test model from the south. Values of ρ_m are shown on the blocks. OPs are shown on the plane $Z = 0$, with the respective numbers of experimental MTS sites in parentheses. At the top: fault names. Regional structures: 1, Chagan-Uzun block; 2, Chuya basin; 3, South Chuya horst; 4, Caledonides of the Tuva TSAs.

impedances $Z_m^{\max H}$, $Z_m^{\min H}$ aligned along the axes X and Y of the model;

– 3D inversion of matrix components $[Z_{ob}]$ and $Z_{ob}^{\max H}$, $Z_{ob}^{\min H}$ was performed for MTS profiles of Ukok–Sagly and Biisk–Tashanta, whose directions matched the axes X and Y in the test model;

– the relationship of the obtained $\rho_{in}(h_{in})$ values with locations of earthquake hypocenters and zones with increased absorption of earthquake converted waves was analyzed.

These stages also included calculation of experimental and model-based 3D asymmetry parameters of impedance matrices $[Z_{ob}]$ and $[Z_m]$, as well as orientation of impedances $Z_{ob}^{\max H}$, $Z_{ob}^{\min H}$ and $Z_m^{\max H}$, $Z_m^{\min H}$.

ESTIMATED POTENTIAL OF 3D INVERSION BASED ON TEST MATRICES $[Z_M]$ AND THEIR INVARIANTS $Z_m^{\max H}$, $Z_m^{\min H}$

Maximum and minimum induction method. Polar impedance diagrams $Z_{xy}(\alpha)$ typically used for determining main directions and impedances are adequate for 2D environs, whereas minima of additional $Z_{xx}(\alpha_1)$ in 3D conditions quite often do not match with the extreme values of main impedances $Z_{xy}(\alpha_2)$, i.e., $\alpha_1 \neq \alpha_2$, and it is unclear what impedances we need to invert. Apparently not taking into account a part of energy transitioning into additional impedances reduces the resolution of the subsurface parameters in case of 1D–2D inversion of MTS curves.

Among all techniques available for diagonalization of the impedance matrix, the method of maximum and minimum induction (Council et al., 1986) is the one that ensures reliable identification of $\theta_H^{\max H}$ and $\theta_H^{\min H}$ directions of maxi-

imum $Z^{\max H}$ and minimum $Z^{\min H}$ impedances for orthogonal real vectors $\mathbf{1H}^{\max}$ and $\mathbf{1H}^{\min}$. The advantage of this algorithm is that if the upper-level dimension is wanton, the lower level is two-dimensional, and the directions of regional 2D structures at the lower level are close to $\theta_H^{\max H}$ and $\theta_H^{\min H}$, then at low phase frequencies we obtain $\text{Arg}Z^{\max H, \min H} \approx \text{Arg}Z^{\perp, \perp}$ for longitudinal and transverse impedance phases, which describe the lower structural level (Belyavsky, 2017). The use of the latter allows us to remove the effects of non-uniformities from the upper part of the subsurface and estimate the parameters of the lower part of the geoelectric model as a result of their 2D inversion.

Adjustment of WSINV3DMT software to geoelectric models of the southern part of the Altai–Sayan region.

The WSINV3DMT software relies on the Occam razor principle, according to which the mismatch function between the experimental and model-based MT data is minimized in a way that produces the smoothest lateral distribution of anomalies $\rho_{in}(h_{in})$. To take into account the distorting effect of nonuniformities from the upper level on the MTS curves, we set their parameters in the starting model, which provides the initial approximation for minimization of the mismatch function. The parameters of blocks in the model, sizes of nodes and their quantities along the coordinate axes were altered in course of testing. 3D inversion for the test model was performed in the period range $0.0018 < T < 95$ s along two parallel profiles simultaneously (Fig. 4a, b). The 3D test model (Fig. 2) constructed for the Biisk–Tashanta (MTS 167–138–88), Ukok–Sagly (MTS 777–1), and Sagly–Shira (MTS 191–221) profiles was taken from (Belyavsky, 2017).

In the test model, we inverted impedances of the matrices $[Z_m]$ and $Z_m^{\max H}$, $Z_m^{\min H}$ calculated using the Maxwell software

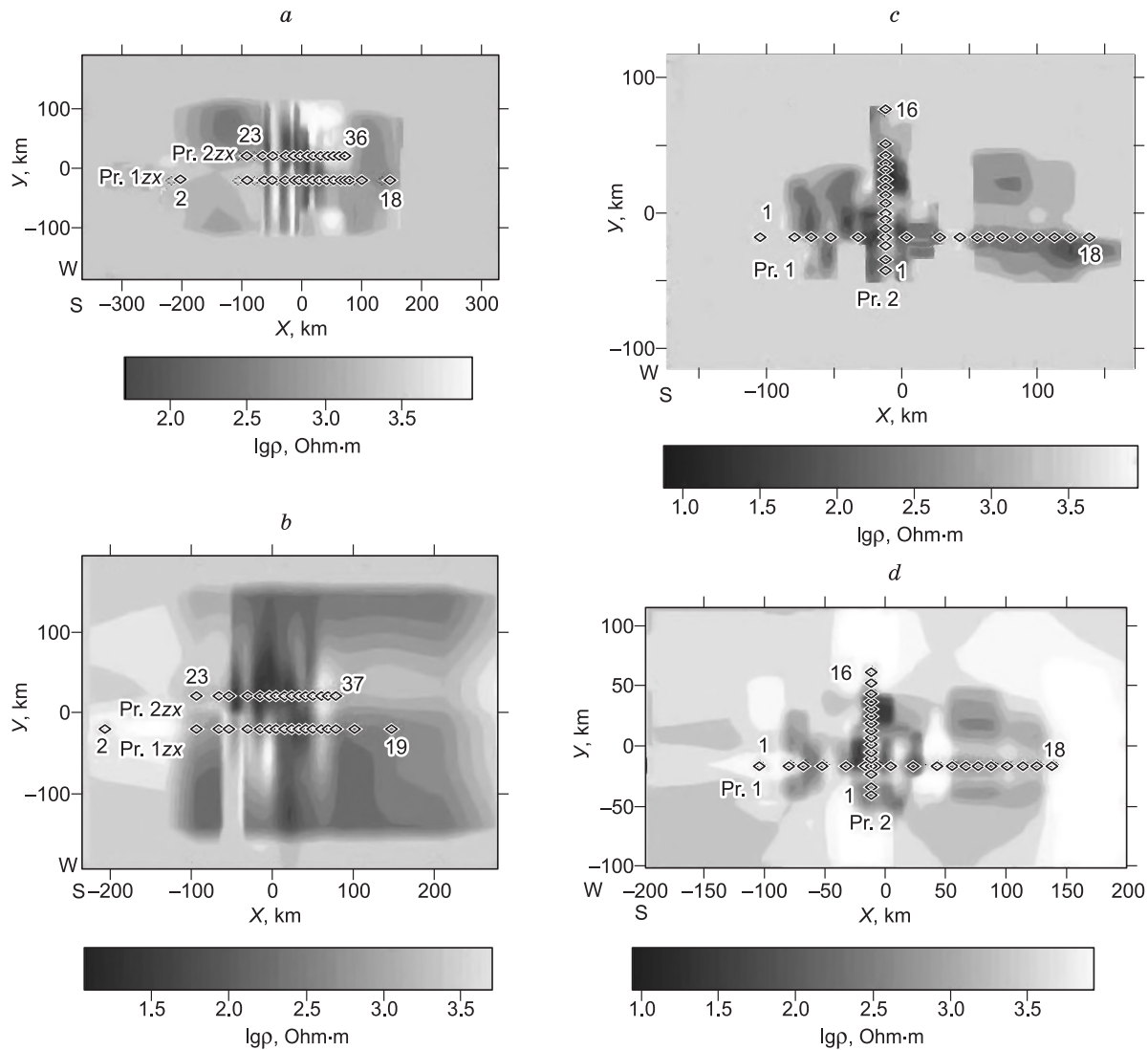


Fig. 4. Distribution of resistivity values in the upper layers of the starting models 1, 4 for Z : 450 m in model 1 (a), 250 m in model 2 (b), 200 m in model 4 (c), 450 m in model 3 (d). Numbers of profiles and the first and last OPs are shown on the maps.

at 31 observation points (OPs) (Fig. 4a) and 33 OPs (Fig. 4b) along profiles 1zx ($Y = 22$ km) and 2zx ($Y = 70$ km) (Fig. 2a). In starting model 1, we studied impedances at OPs 2–18 along profile 1zx and OPs 23–36 along profile 2zx, and in model 2—impedances at OPs 2–19 along profile 1zx and OPs 23–37 along profile 2zx. The parameters of the upper layer in model 1 and those of the superimposed layer in model 2 are presented in the second and the third columns of the Table 1. The number of iterations and 3D inversion error, i.e., RMS parameter, are also shown. In these starting models, impedances Z_{in}^{yx} and Z_{in}^{xy} obtained as a result of 3D inversion agree best with $[Z_m]$ and $Z_m^{\max H}$, $Z_m^{\min H}$. The parameters of the starting models 3 and 4 used for inversion of impedances $[Z_{ob}]$ and $Z_{ob}^{\max H}$, $Z_{ob}^{\min H}$ are presented in the last two columns of the Table 1.

Inversion of $[Z_m]$ matrix components. Resistance distribution in the upper part of the starting model 1 (Fig. 4a)

matched the ρ_m values of the test model (Fig. 2a), which took into account the effect of nonuniformities from the upper layer on the $[Z_m]$ matrix components obtained as a result of 3D inversion. It can be seen from Fig. 5 that 3D inversion maps the locations of conductive faults and blocks in the upper part of the model, but it underestimates depths h_m to the lower conductive blocks located below OPs 2–4 and 14–19 along profile 1zx. In addition, the anomalies caused by the conductive blocks underlying profile 2zx occur (Fig. 5b).

In profile 2zx, anomalies with $\rho_m(h_m) = 10\text{--}40$ Ohm·m partially match the locations of the model blocks with $\rho_m = 10\text{--}20$ Ohm·m at the depth $h_m = 10\text{--}20$ km, but the anomalies below OPs 32, 33, 36 are caused by the low-resistivity blocks located below OPs 12 and 16 in profile 1zx (Fig. 5). Thus, the match between the distribution maps of $\rho_m^{xy}(T)$ and $\rho_m^{yx}(T)$ values from the inversion and model-based $\rho_m^{xy}(T)$ and

Table 1. Distributions of starting model parameters and inversion errors (RMS)

| Parameter | Model | | | |
|---|--|--|--|---|
| | 1 | 2 | 3 | 4 |
| Numbers of nodes along axes X, Y, and Z; iterations; RMS | 41, 20, 20; 19 iterations; RMS < 3 | 41, 20, 20; 16 iterations; RMS ≈ 4 | 43, 26, 20; 15 iterations; RMS ≈ 6 | 43, 26, 20; iterations 15; RMS ≈ 5 |
| Resistivity values in the upper layer of the starting 3D model, Ohm·m | 200, 3000, 4000, 500, 1000, 200, 10,000 | 200, 1000, 20, 4000. Layer is superposed by a quasi-uniform layer with $\rho_m = 200$ and 1000 | 200, 4000, 1000, 10,000. Layer is superposed by a quasi-uniform layer with $\rho_m = 200$ and 1000 | 200, 4000, 1000, 10,000 |
| Thicknesses of layers 1 and 2 and sizes, km | $H_1 = 1.1$ along $Y = 220$, $X = 600$ | $H_1 = 0.2, H_2 = 1.1$, along $Y = 300, X = 510$ | $H_1 = 0.3, H_2 = 1.1$ along $Y = 90, X = 240$ | $H_1 = 1.1$ along $Y = 90$, $X = 255$ |

$\rho_m^{yx}(T)$ presented in Fig. 6, as well as low RMS values, do not guarantee that $\rho_{in}(h_{in})$ and $\rho_m(h_m)$ values located strictly below the profile line will be close due to the observed lateral sounding effect.

Inversion of Z_m^{maxH} and Z_m^{minH} impedances. Before 3D inversion of Z_m^{maxH} and Z_m^{minH} impedances was performed, their orientations with respect to axes X and Y were assessed (Fig. 2). This allowed us to find out whether they match the impedances Z_{xy} or Z_{yx} inverted in WSINV3DMT software. We can see that $|Z_m^{maxH}|$ and $|Z_m^{minH}|$ for profile 1zx have orientations close to those of X and Y axes with deviations not exceeding 10°–20°, however, in case of profile 2zx the deviations may reach 50°.

3D inversion of Z_m^{maxH} and Z_m^{minH} (Fig. 7) for starting model 2 was performed for a uniform surface layer with underlying blocks (Fig. 4b) and the resistivity values matching the ρ_m distribution in the test model (Fig. 2a). Introduction of a uniform upper layer makes it possible to smooth the effects of nonuniformities in the form of contrasting ρ_m changes in the upper part of the test model for the impedances obtained during 3D inversion (Miensopust et al., 2013).

In case of profile 1zx, the $\rho_{in}(h_{in})$ section obtained as a result of 3D inversion of impedances Z_m^{maxH} and Z_m^{minH} agrees with locations of the lower conductive blocks in the test model, except for OPs 2–4, where, similarly to the inversion of $[Z_m]$ matrix components, a conductivity anomaly occurs to be caused by the block located below profile 2zx. In profile 2zx, anomalies $\rho_{in}(h_{in})$ below OPs 29–33 are either shifted upward with respect to $\rho_m(h_m)$ or are absent, similarly to the inversion of all $[Z_m]$ matrix components.

Conclusions. 3D inversion of all $[Z_m]$ matrix components or impedances Z_m^{maxH} and Z_m^{minH} recovers locations of low-resistive blocks in the upper part of the subsurface and with a margin of error faults. Locations of the lower conductive blocks in Profile 1zx are mapped by inversion of Z_m^{maxH} and Z_m^{minH} under the starting model 2. 3D inversion of $[Z_m]$ matrix components under starting model 1 partially recovers the locations of the lower conductive blocks only for profile 2zx. 3D inversions of $[Z_m]$ or Z_m^{maxH}, Z_m^{minH} are accompanied by anomalies with decreased $\rho_{in}(h_{in})$ caused by the blocks remote from the OPs (along the Y axis), while a high-resistivity layer is mapped below the low-resistivity anomalies

$\rho_{in}(h_{in})$ at the depth $h_{in} \approx 40$ –50 km, which is absent in the test model (Figs. 5, 7).

3D INVERSION OF EXPERIMENTAL MATRICES $[Z_{OB}]$ AND THEIR INVARIANTS $Z_{ob}^{maxH}, Z_{ob}^{minH}$

Inverted MTS curves. Ukok–Sagly profile (MTS 777–1) extends at angles of 50°–70° to deep faults (Fig. 1). Impedances Z_{ob}^{maxH} at MTS sites 777–732 are oriented along azimuth $Az = 30$ –50°, i.e., almost orthogonally to fault strikes, and thus we have $Z_{ob}^{maxH} \approx Z^{\perp}$. At the center of the basin and at its eastern edge (MTS 731–49), azimuths Az vary from 0° to 90°. At the remaining MTS sites, Z_{ob}^{maxH} have orientations close to that of the X axis. Along Biysk–Tashanta profile, impedances Z_{ob}^{maxH} are oriented along azimuth $Az = -10$ –(–60°) at MTS sites 68–72, i.e., $Z_{ob}^{maxH} \approx Z_{yx}$, while changes in limits $Az = (-50^{\circ}) - (-100^{\circ})$ at MTS sites 73–91. The profile segment between MTS 92 and MTS 107 passes near the Kurai fault, and thus we have $Z_{ob}^{maxH} \approx Z^{\perp}$ (Belyavsky, 2017).

As a result, impedances Z_{ob}^{maxH} and Z_{ob}^{minH} along Ukok–Sagly and Biisk–Tashanta profiles predominantly show orientations close to those of X and Y axes with azimuths 60° and –30°. If $|Z_{ob}^{maxH}|$ and $|Z_{ob}^{minH}|$ are significantly different and their orientations deviate from these azimuths by over 20°–30°, then they are discarded. This made it possible to test the potential of 3D inversion of impedances Z_{ob}^{maxH} and Z_{ob}^{minH} using the impedances Z_{xy} and Z_{yx} inverted by WSINV3DMT software. The arithmetic mean relative errors between the regular and control observations for ρ_{ob}^{xy} and ρ_{ob}^{yx} curves were on average 0.073 and 0.078, while the arithmetic mean errors of phase identification were 3.3° for $ArgZ_{xy}$, and 1.6° for $ArgZ_{yx}$.

To recover the geoelectric parameters of the blocks at the lower level, the shift effect of local nonuniformities from the upper level on MTS curves should be removed (Jones, 1988). To suppress the manifestations of the “shift effect” during 3D inversion, we plotted the arithmetic mean curves for groups of quasi-conformal $\rho_{ob}^{maxH}(T), \rho_{ob}^{minH}(T)$ and $\rho_{ob}^{xy}(T), \rho_{ob}^{yx}(T)$. The experimental curves included in these groups after discarding the curves with $\rho_k(T)$ values significantly dif-

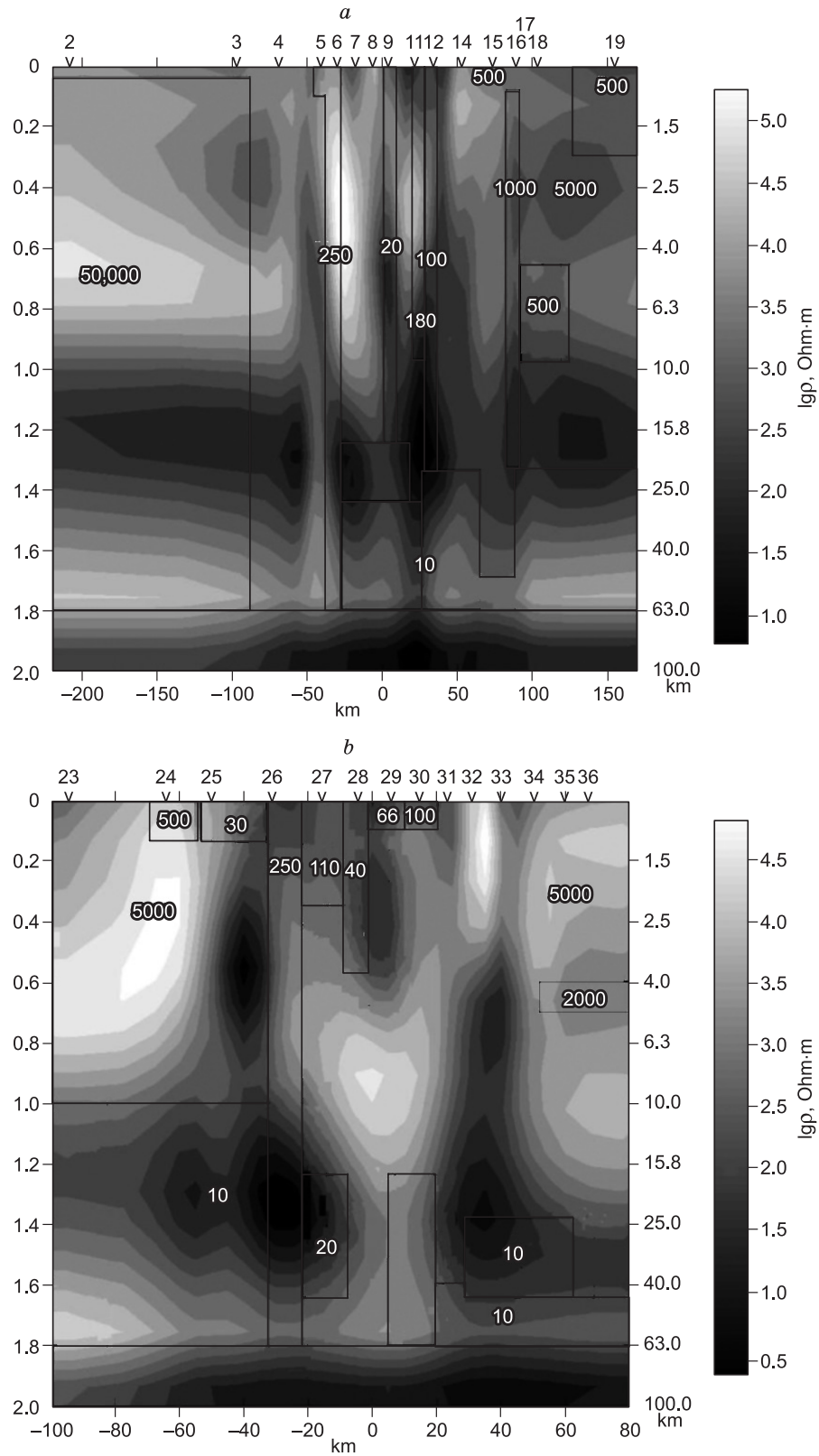


Fig. 5. Geoelectric sections obtained as a result of 3D inversion of $[Z_m]$ components for the starting model 1 along the profiles: *a*, 1zx, *b*, 2zx. At the top: OP numbers. Lines indicate locations of blocks in the test model. On the right: resistivity scale in l_{gp} (Ohm·m). Depths are shown on a logarithmic scale on the left from the sections and on a linear scale on the right.

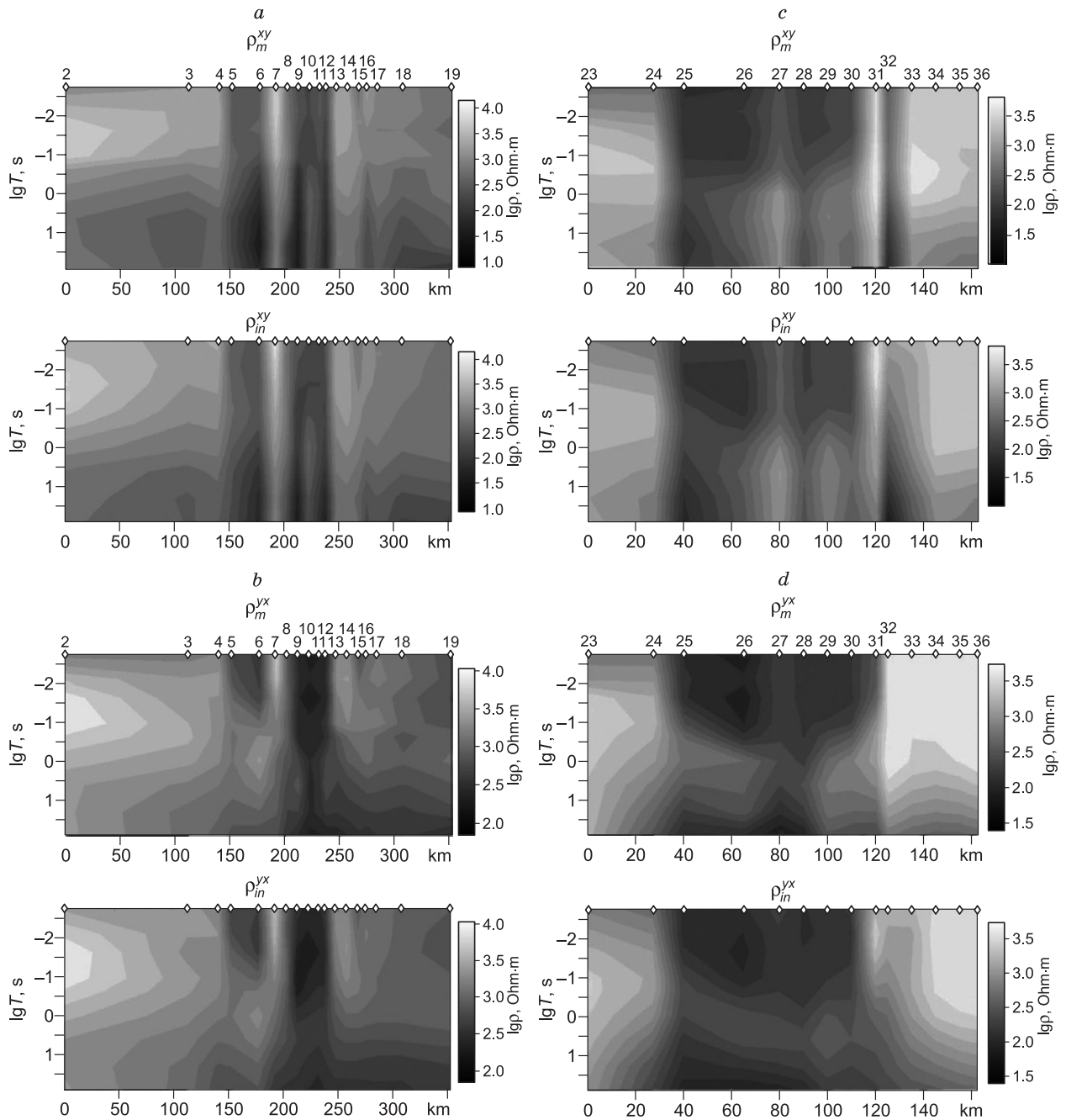


Fig. 6. Distribution of inverted apparent resistivities $\rho_m^{xy}(t)$, $\rho_m^{yx}(t)$ (upper maps) and the ones obtained as a result of 3D inversion $\rho_{in}^{xy}(t)$, $\rho_{in}^{yx}(t)$ (lower maps) along Profile 1zx (a, b) and Profile 2zx (c, d) for: $\rho_m^{xy}(a, c)$, $\rho_m^{yx}(b, d)$. At the top: OPs and their numbers. On the right: ρ_{in} scale in $\lg\rho$ (Ohm·m).

ferent from the arithmetic mean values $\bar{\rho}_k(T)$ of the respective groups were averaged by periods. The shift effect was significantly reduced in the obtained $\rho_k(T)$ curves. These groups of MTS data matched the OPs, at which impedances $[Z_{ob}]$ or \check{Z}_{ob}^{maxH} , \check{Z}_{ob}^{minH} were inverted within the period range $0.0144 < T < 240$ s.

Along the Ukok–Sagly (MTS 772–7) and Tashanta–Bisk (MTS 66–107) profiles, they are combined into 18 (profile 1) and 16 (profile 2) groups, respectively, which are rep-

resented above the resulting $\rho_{in}(h_{in})$ sections (Figs. 8 and 9) and in the starting models 3 and 4 (Fig. 4c, d). 3D inversion of experimental matrices $[Z_{ob}]$ or \check{Z}_{ob}^{maxH} , \check{Z}_{ob}^{minH} oriented along the X and Y axes is performed for these groups (Fig. 1).

Starting model parameters. The starting 3D models took into account the results of 1D inversion of impedances Z_{ob}^{maxH} (Figs. 8c and 9c). The parameters of the starting models 3 and 4 (Fig. 4c, d), for which the curves $\rho_m^{yx}(T)$ and $\rho_{in}^{xy}(T)$ obtained as a result of the 3D inversion agree best with

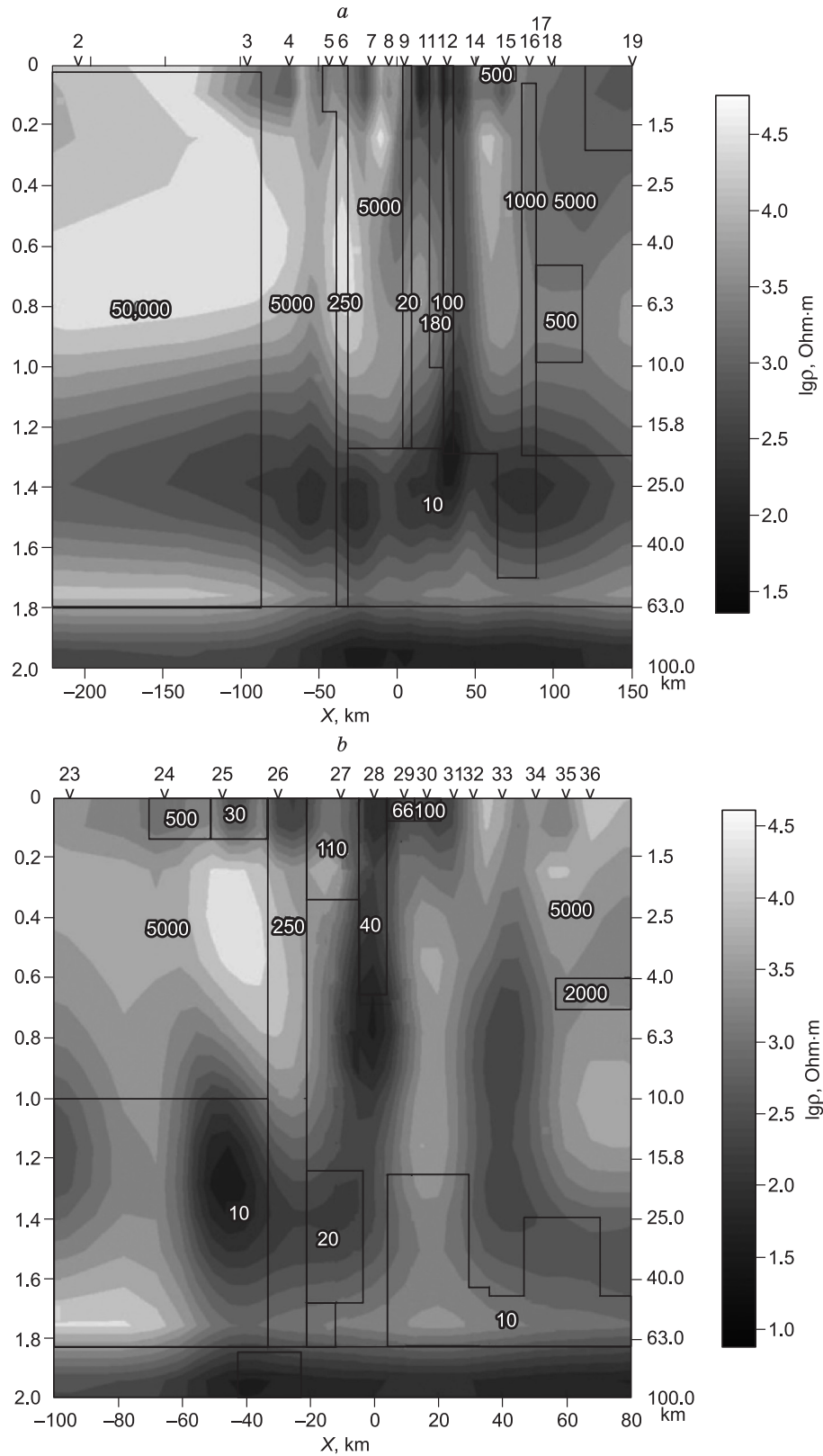


Fig. 7. Geoelectric sections along Profile 1zx (a) and Profile 2zx (b) obtained by 3D inversion of impedances $Z_m^{\max H}$ and $Z_m^{\min H}$ under the starting model 2. See the legend in Fig. 5.

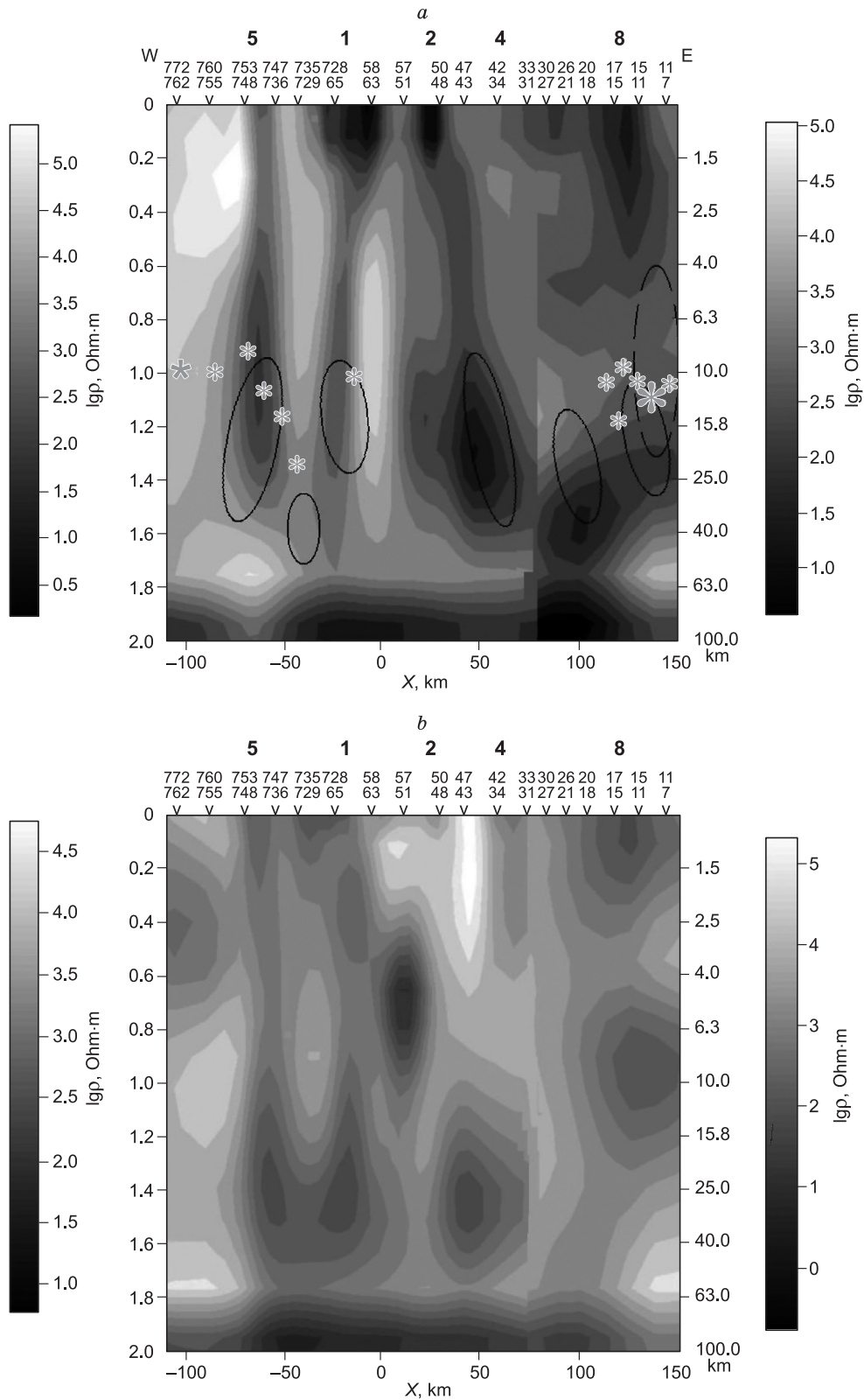


Fig. 8. Ukok–Sagly profile. 3D inversion results for the following starting models: *a*, 3, \check{Z}_{ob}^{maxH} and \check{Z}_{ob}^{minH} ; *b*, 4, [\check{Z}_{ob}] component; *c*, results of 1D inversion of impedances Z_{ob}^{maxH} . Resistivity values are shown on the left for the maps in the left part of the MTS profile, and on the right for the right part. Numbers at the top are the numbers of MTS sites in groups and deep faults (Fig. 1). Depths are shown on logarithmic (on the left) and linear (on the right) scales. White stars are hypocenters of earthquakes with $M = 1.5\text{--}3.3$ recorded during studies of earthquake converted waves (2006–2008), the large star is the hypocenter of the Uureg Nuur earthquake with $M = 7.0$ (1970). Ellipses: solid lines indicate absorption of converted waves of earthquakes with $K > 0.0009$ dB/km, dashed lines indicate earthquake concentration areas (Emanov et al., 2012). White lines indicate activated faults, and black lines indicate faults identified from earthquake converted waves (*c*).

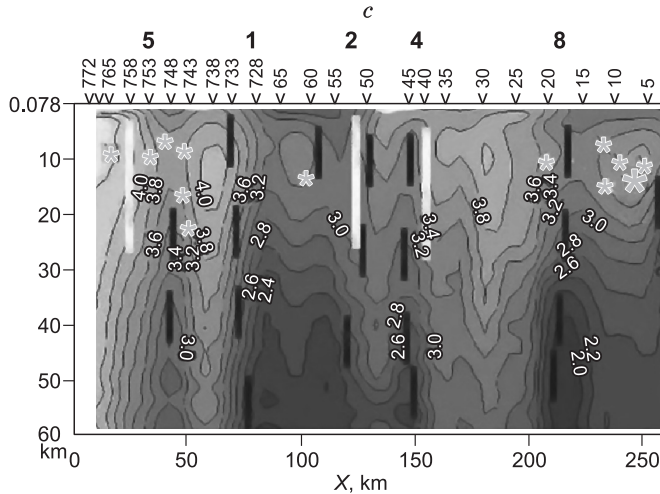


Fig. 8. (continued).

$\rho_{ob}^{xy}(T)$, $\rho_{ob}^{yx}(T)$ and $\rho_{ob}^{\max H}(T)$, $\rho_{ob}^{\min H}(T)$, are presented in the Table 1. Resistivity distribution in the upper layer in model 4 is close to ρ_m in the upper part of the test model, while in model 3 it is superimposed by a quasi-uniform bed.

During 3D inversion, cell sizes along X and Y axes at the central part of the test model were 5–6 km, while at the periphery they reached 60–100 km. We defined 43 cells along the X axis and 26 along the Y axis. Sizes of 20 cells along the Z axis increased from 100 m ($Z = 0$ km) to 50 km ($Z = 170$ km). The length of the starting models along the X axis was 520 km and along the Y axis 380 km. The calculations took 16–20 iterations. It took less than 24 hours to perform inversion of all $[Z_{ob}]$ components on the specified period grid on a 2.7 GHz PC with 4 GB RAM.

Geoelectric models of Altai and Shapshal focal zones of earthquakes. The results of the 3D inversion of $[\check{Z}_{ob}]$ components and impedances $\check{Z}_{ob}^{\max H}$ and $\check{Z}_{ob}^{\min H}$ along the Ukok–Sagly profile show (Fig. 8) a series of anomalies with $\rho_{in} = 100$ –200 Ohm·m at the depths of 4 to 20 km in the segment between South Terekta and Shapshal faults. Subsurfaces $\rho_{in}(h_{in})$ are close to $\rho_m(h_m)$ of the test model in Fig. 2b at depths up to $h_{in} \approx 10$ –15 km, but the $\rho_{in}(h_{in})$ isolines below 20 km do not map a monolithic conductive lithosphere, which spreads to the depths of 100 km, as $\rho_m(h_m)$ in the test model. Positions of deep conductivity anomalies obtained for $\check{Z}_{ob}^{\max H}$, $\check{Z}_{ob}^{\min H}$ and $[\check{Z}_{ob}]$ are often shifted. Differences in sizes of $\rho_{in}(h_{in})$ anomalies can be observed as well. Since testing of WSINV3DMT software showed that it is more reasonable to invert $Z_m^{\max H}$ and $Z_m^{\min H}$ under the starting model 2 along profile 1x, the results of inversion of $\check{Z}_{ob}^{\max H}$ and $\check{Z}_{ob}^{\min H}$ were analyzed (Fig. 8b).

The 3D inversion of impedances $\check{Z}_{ob}^{\max H}$ and $\check{Z}_{ob}^{\min H}$ along Bimsk–Tashanta profile (Fig. 9a) below the MTS sites 67–107, identified three near-vertical conductive anomalies with $\rho_{in} = 200$ –300 Ohm·m at depths $h_{in} \approx 3$ –4 km that ex-

tended to the depths $h_{in} = 20$ –30 km. Inversion of $[\check{Z}_{ob}]$ components shows $\rho_{in}(h_{in})$ anomalies (Fig. 9b) characterized by $\rho_{in} = 30$ –50 Ohm·m in the depth range from $h_{in} = 4$ –6 km to $h_{in} = 15$ –25 km, which is lower than ρ_{in} obtained from inversion of $\check{Z}_{ob}^{\max H}$ and $\check{Z}_{ob}^{\min H}$.

Switching to starting model 3 during the inversion of $[\check{Z}_{ob}]$ components shows conductive anomalies that are close, but slightly shifted with respect to the ones obtained from starting model 4. The resulting model in Fig. 9a correlates with locations of zones with increased absorption of earthquake converted waves. This was the model considered for geological explanation of the identified conductive objects.

Comparison of maps the inverted apparent resistivity values $\rho_{ob}^{xy}(T)$, $\rho_{ob}^{yx}(T)$, $\rho_{ob}^{\max H-\min H}(T)$ and $\rho_{in}^{xy}(T)$, $\rho_{in}^{yx}(T)$ along the Ukok–Sagly profile shows (Fig. 10) that they closely match. Curves $\rho_{ob}^{\max H-\min H}(T)$ agree with the orientations of $\rho_{ob}^{\max H}(T)$ or $\rho_{ob}^{\min H}(T)$ curves, which are close to that of the X axis for the obtained $\rho_{in}^{xy}(T)$ (Fig. 10c) or Y axis for $\rho_{in}^{yx}(T)$ (Fig. 10d).

Reliability of geoelectric sections plotted for MTS sites 67–107 (profile 2) may be assessed based on arithmetic mean relative errors $\delta^{\max H-\min H}$ (calculated for all periods) and $\delta^{\text{Arg}yx}$, $\delta^{\text{Arg}xy}$, i.e. the average deviations of $\text{Arg}Z_{xyin}$ from $\text{Arg}\check{Z}_{ob}^{\max H}$, $\text{Arg}\check{Z}_{ob}^{\min H}$ (Fig. 11). We can see that the error of matching curves $\rho_{in}^{xy}(T)$, $\rho_{in}^{yx}(T)$ to $\rho_{ob}^{\max H-\min H}(T)$ is $\delta^{\max H-\min H} < 0.5$, which is lower, than the error (δ^{xy-yx}) of fitting curves $\rho_{in}^{xy}(T)$, $\rho_{in}^{yx}(T)$ to $\rho_{ob}^{xy}(T)$, $\rho_{ob}^{yx}(T)$. Therefore, the information from geoelectric sections plotted based on impedances $\check{Z}_{ob}^{\max H}$ and $\check{Z}_{ob}^{\min H}$ is at least equally reliable, as from inversion of $[\check{Z}_{ob}]$ components.

We can see from the distribution of $\rho_{in}(h_{in})$ maps (Fig. 12) that ER values at the depth of 24.6 km in the deep fault zone of the Chuya and Shapshal epicenter fields decreases to 10–100 Ohm·m. In the latter case, the conductivity maximum is located to the south of the MTS line near the epicenter of the Ureg–Nur earthquake. We can see that ρ_{in} increases up to 50–200 Ohm·m at the depth of 42 km within fault and focal zones of earthquakes in the eastern part of profile 1 and up to 300–400 Ohm·m in the north of profile 2 (Fig. 12c).

Geoelectric sections in Figs. 8 and 9 are different from the test model, as they lack the conductive bed extending from depths of 20–30 km to 80 km and below. They match closely with the earthquake focal model presented in (Belyavsky and Rakitov, 2012) and agree with the model characterized by fluid generation in the consolidated crust, the presence of a conductive layer at $h = 15$ –40 km, and the base extending to depths of 40–60 km (Van’yan, 1997). Deep faults with E and NE strike directions are characterized by ρ_{in} decreasing down to 100–300 Ohm·m along pro-

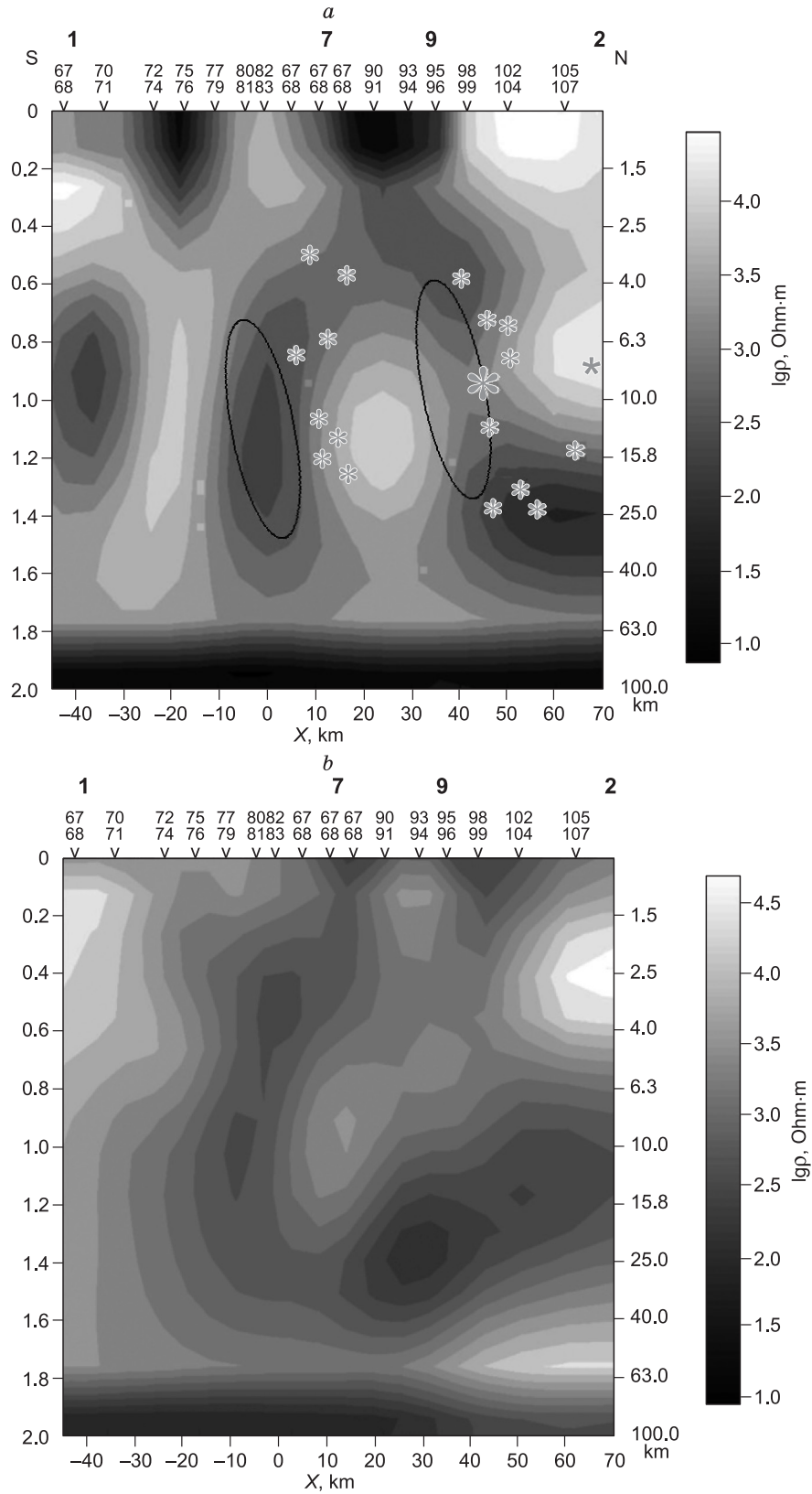


Fig. 9. Biisk–Tashanta profile (MTS 67–106). 3D inversion results for the following starting models: *a*, 3, impedances \check{Z}_{ob}^{maxH} and \check{Z}_{ob}^{minH} ; *b*, 4, $[\check{Z}_{ob}]$ components; *c*, 1D inversion of $|Z_{ob}^{maxH}|$ curves. Large star—hypocenter of the Altai (Chuya) earthquake with $M = 7.3$ (2003). 9 Resistivity—deep fault identified using the method of earthquake converted waves. See the legend in Fig. 8.

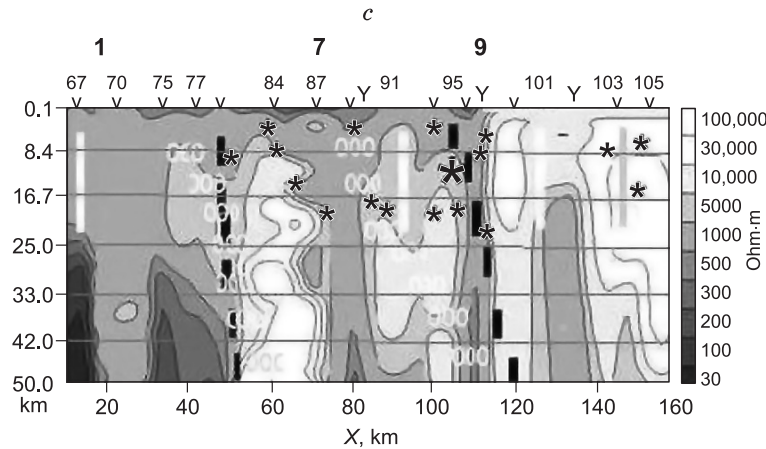


Fig. 9. (continued).

file 2 (Fig. 9), and the ones with NW strike directions show the decrease down to 10–50 Ohm·m along profile 1 (Fig. 8) with respective increase in liquid fraction content.

RESEARCH RESULTS

1. Adjustment of the 3D inversion of components of the impedance matrix $[Z_m]$ embedded in the WSINV3DMT software to inversion of induction impedances $Z_m^{\max H}$ and $Z_m^{\min H}$ using the test model demonstrated that the proposed method makes it possible to recover geoelectric structures with slight shifts. The method provides reliable maps (Figs. 5 and 7) of low-resistivity blocks in the upper part of the section, as well as conductive faults. However, the base of deep high-conductivity anomalies is located above the base of the predetermined blocks with high conductivity σ_m . This may be a manifestation of the equivalence principle, i.e., given the identical integral conductivities of the blocks, inversion of components of the impedance matrix may reduce their thicknesses, while simultaneously reducing ρ_{in} values as well. We may observe splitting of the middle crustal layers into a series of isolated conductivity anomalies in $\rho_{in}(h_{in})$ values.

It follows from $\rho_{in}(h_{in})$ distribution maps that low resistivity anomalies may be also caused by the effect of low-resistivity blocks remote from the studied OPs (along the X axis) on profiles 1zx or 2zx (Fig. 2). In other words, a lateral sounding phenomenon takes place. Deep blocks with low ρ_m along profile 1zx are better mapped by $\rho_{in}(h_{in})$ anomalies obtained as a result of 3D inversion of impedances $Z_m^{\max H}$ and $Z_m^{\min H}$ under the starting model, which is characterized by presence of a thin uniform layer near the surface superposed over the layer with ρ_m values agreeing with the resistivity distribution in the upper part of the test model (Figs. 7 and 4b). Inversion of $[Z_m]$ components is accompanied by upward movement of the lower conductive $\rho_{in}(h_{in})$ anomalies with respect to the predetermined model blocks with high conductivity (Fig. 5a).

Conclusions. Inversion of impedances $Z_m^{\max H}$ and $Z_m^{\min H}$ under the starting model, which takes into account conductivity changes in the upper part of the test model, performs comparably to the inversion of all $[Z_m]$ components in terms of recovering parameters of the conductive blocks.

2. 3D inversion of experimental matrices $[\check{Z}_{ob}]$ or $\check{Z}_{ob}^{\max H}$, $\check{Z}_{ob}^{\min H}$ not always identifies the same model blocks as interactive matching of 3D model $\rho_m^{\max H}(T)$, $\rho_m^{\min H}(T)$ curves and $\rho_{ob}^{\max H}(T)$, $\rho_{ob}^{\min H}(T)$ curves (Fig. 2). For example, conductivity anomalies along Ukok–Sagly profile are isolated and manifest themselves at depths from $h_{in} = 10$ –20 km to 40 km (Fig. 9), while in the test model they appear at depths from $h_m = 20$ –30 km to 80 km in the form of fused conductive blocks. Moreover, a high-resistivity layer occurs under the conductive blocks at depths below 40–50 km, which is absent in the model in Fig. 2.

Apparent resistivities $\rho_{ob}^{\max H}(T)$, $\rho_{ob}^{\min H}(T)$ are close to ρ_{in}^{xy} and ρ_{in}^{yx} values at most OPs (Figs. 10 and 11), if ρ_m and h_m values in the near-surface layer in the starting model are close to the ones obtained by interactive fitting of $\rho_m^{\max H}(T)$, $\rho_m^{\min H}(T)$ curves to $\rho_{ob}^{\max H}(T)$, $\rho_{ob}^{\min H}(T)$ curves, and this near-surface layer is superposed by a thin quasi-uniform layer. However, close values do not guarantee the reliable recovery of geoelectric parameters in deep subsurface areas.

Conclusions. 3D geoelectric models constructed by interactive fitting of model-based MTS curves to the experimental curves should be adjusted by 3D inversion of $\rho_{ob}^{\max H}(T)$, $\rho_{ob}^{\min H}(T)$ curves, with changes in resistivity values in the upper part of the section taken into account.

3. Earthquake hypocenters underlying Biisk–Tashanta profile (Fig. 9) are concentrated at depths of 4–25 km near low-resistivity faults with $\rho_{in} \approx 200$ –50 Ohm·m, which bound the Chagan-Uzun horst in the north and in the south. These anomalies with low $\rho_{in}(h_{in})$ match the areas with increased absorption of earthquake converted waves, which indicates their common nature. The hypocenter of the Altai

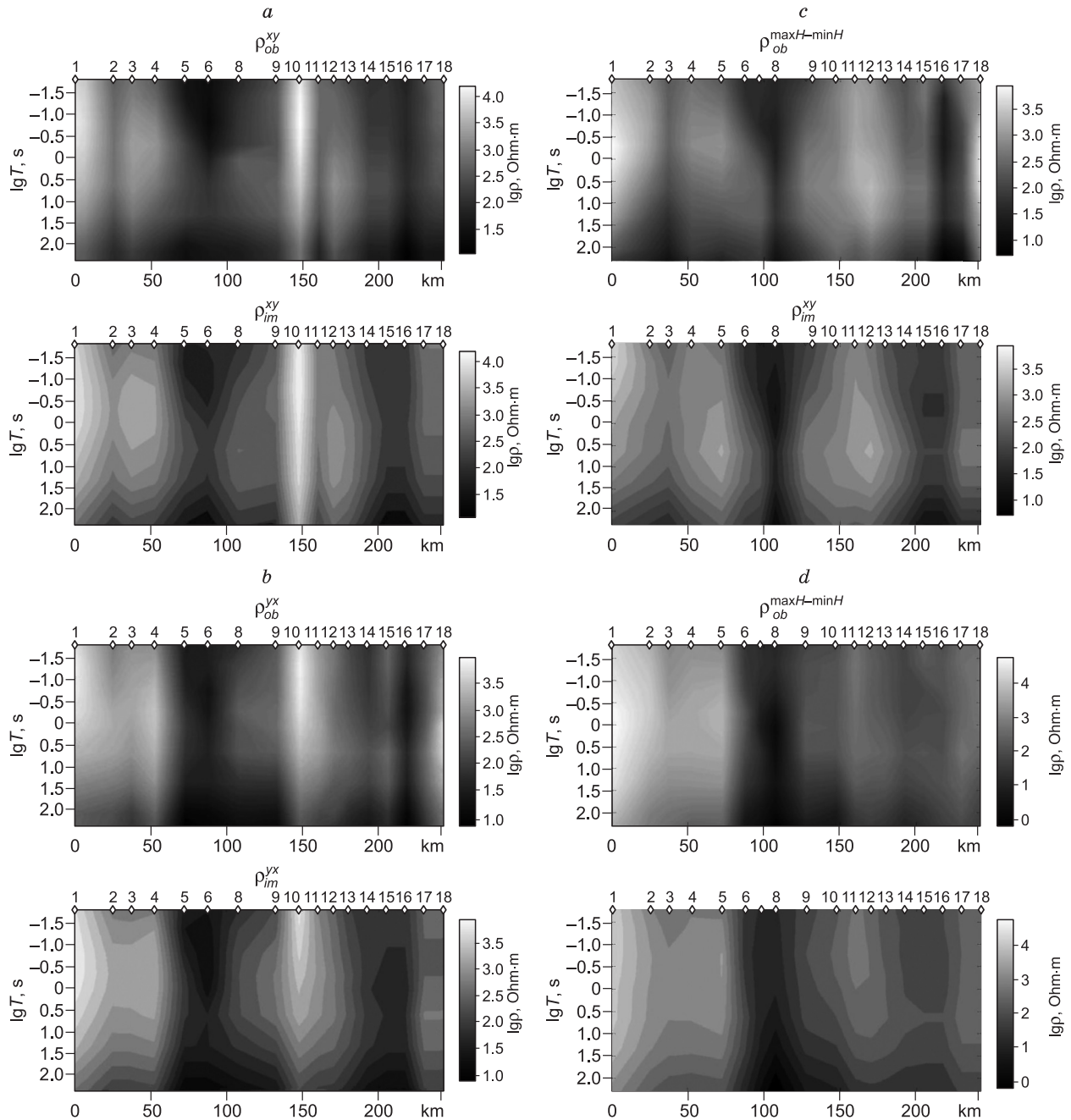


Fig. 10. Pseudosections of the experimental values ρ_{ob}^{xy} (a), ρ_{ob}^{yx} (b), and $\rho_{ob}^{maxH-minH}$ (c, d) (upper maps) and obtained values ρ_{in}^{xy} , ρ_{in}^{yx} (lower maps) along the Ukok—Sagly profile for starting models 4 (a, b) and 3 (c, d). At the top: OP locations and numbers. On the right: resistivity scale.

earthquake is located above the zone with gradient decrease in ρ_{in} down to 50–100 Ohm·m (Fig. 9b) near the low-resistivity fault that separates the Kurai basin from the Chagan-Uzun horst. Location of the Shapshal focus correlates with the position of the increased conductivity anomaly (Fig. 12), while hypocenters of the Shapshal focus are also located above the zone with increased conductivity and absorption

of earthquake converted waves (Fig. 8). Earthquake hypocenters are concentrated near Shapshal and South Terekta deep faults (Fig. 8) above the blocks characterized by ρ_{in} decreasing down to 100–300 Ohm·m at the depths of 10–20 km.

Conclusions. Earthquake hypocenter positions are controlled by distribution of increased electrical conductivity in

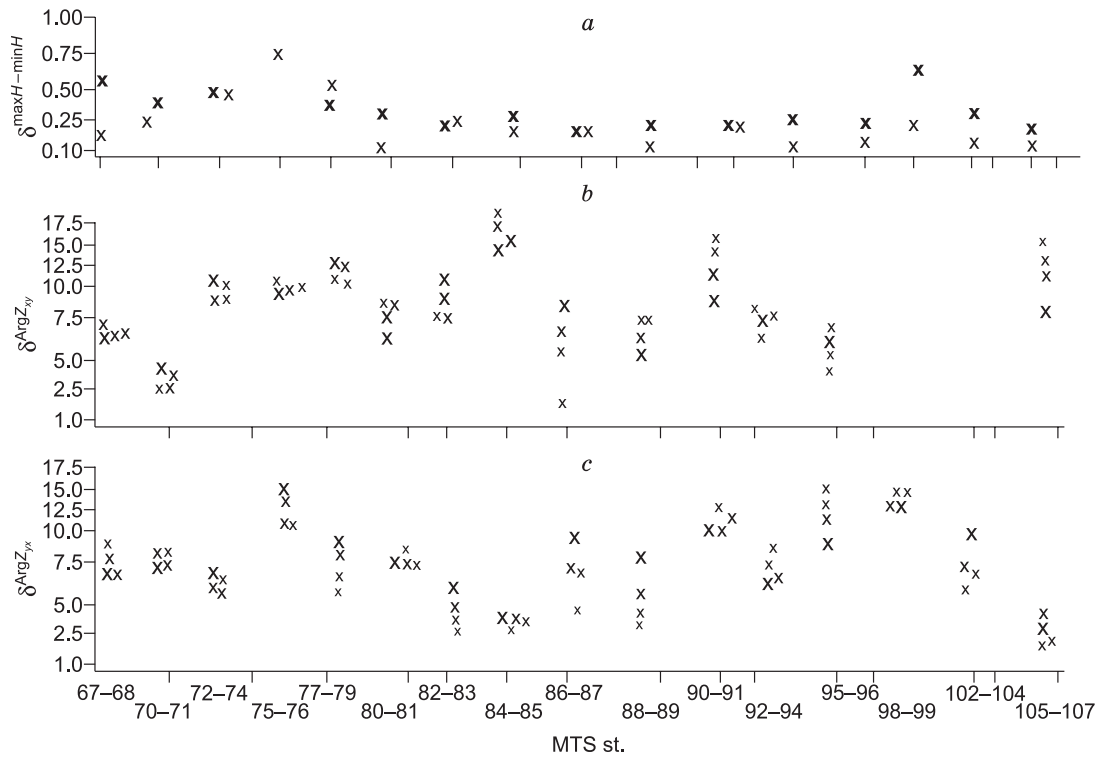


Fig. 11. Biisk–Tashanta profile. Arithmetic mean relative errors for the curves of apparent resistivity values by 3D inversion of impedances: *a*, $Z_{ob}^{maxH-minH}$ (large crosses) oriented along the *X* axis ($\delta_x^{maxH-minH}$) and $Z_{ob}^{maxH-minH}$ (small crosses) oriented along the *Y* axis ($\delta_y^{maxH-minH}$). Differential arithmetic mean errors δ_{xy}^{ArgZ} (*b*) and δ_{yx}^{ArgZ} (*c*) for impedance phases $Z_{ob}^{maxH-minH}$. The calculations are performed for the following period ranges: $0.014 < T < 240$ s, $0.17 < T < 110$ s, $0.17 < T < 22$ s and $0.51 < T < 22$ s and match with decreases in sizes of the stars in parts *b* and *c*.

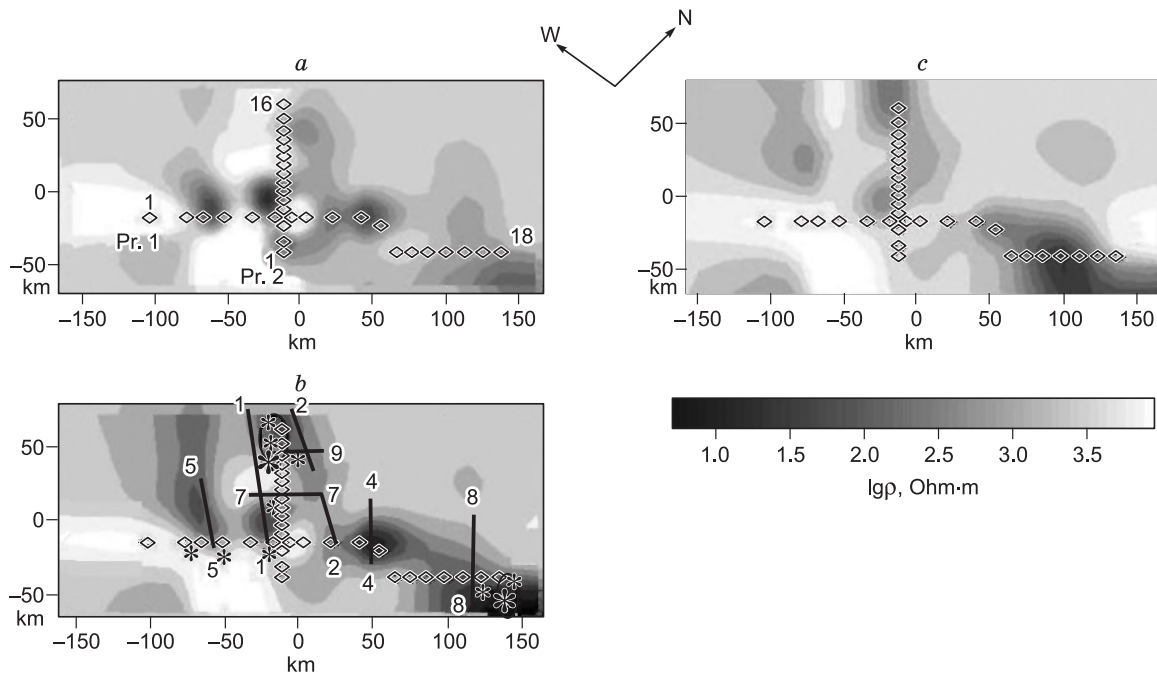


Fig. 12. Distribution maps of ρ_{in} at depths $h_{in} = 10,600$ (*a*), $24,600$ (*b*), and $36,000$ (*c*) m (by 3D inversion of impedances Z_{ob}^{maxH} and Z_{ob}^{minH}). Numbers of the first and the last OPs in the starting models are shown in Fig. 12*a*. Straight lines (*b*)—deep fault locations: 1, 2, 4, 5, 7, 8, 9; stars—earthquake epicenters (Chuya and Ureg Nour earthquakes are shown by large stars), ellipses—earthquake epicenter concentration areas (Liseikin and Soloviev, 2005; Emanov et al., 2012).

the crust, i.e., by zones with increased crust permeability and liquid fraction saturation.

4. South Terekta, Kurai, East Shapshal, Shapshal, and Bashelan deep faults with WNW strike directions are characterized by increased conductivities at various depths (Fig. 8), the ones with NEN strike directions display lower conductivities (Fig. 9). The data on resistivity values in these faults may be used to show that maximum liquid fraction contents at depths of 1–3 km are found in NW trending faults and at the depths of 10–20 km in the blocks underlying the Kurai and Shapshal faults. It is these blocks with increased porosity and water content that the zones with increased absorption of earthquake converted waves are associated with. These findings agree with the conclusions from (Rebetsky et al., 2013), which indicate the E–W stretching evolution of crustal stretching processes within Chuya and Kurai basins and shifts along faults with WNW strike directions. The presence of loosened rocks below the basins is also evidenced by decreased density anomalies Δg in the upper and middle crust (Dobretsov et al., 2016).

3D inversion of the MT data has shown that in the studied area fluid generation occurs in the consolidated crust (the base of the lower conductive blocks is located at depths of 40–50 km). The thermal regime in the studied area of the Altai–Sayan region favors fluid generation at depths of 30 km, where temperatures reach 600–700 °C (Matrosov et al., 1988), which is sufficient for dehydration of rocks of the amphibolite metamorphic facies (Brown and Mussett, 1981) that are present in the rim of the Chuya and Kurai basins (Buslov et al., 2013). Further migration of the generated fluid leads to decrease in ER values in the permeable upper blocks of the crust, near and above which (Figs. 8b and 9a) hypocenters of the studied earthquakes are located.

The author thanks the colleagues from Krasnoyarsk Research Institute of Geology and Mineral Resources and All-Russian Research Institute of Geophysical Exploration Methods who were responsible for field observations and MTS data processing and converted-wave analysis, the Editorial Board of the journal Russian Geology and Geophysics for valuable contributions and corrections made by reviewers, and P.Yu. Pushkarev for his assistance with the adjustment of WSINV3DMT software.

REFERENCES

- Belyavsky, V.V., 2017. 3D Interpretation of Magnetotelluric Data. LAP-LAMBERT Academic Publishing, Saarbrücken, Deutschland.
- Belyavsky, V.V., Rakitov, V.A., 2012. Fluid-filled focal zones earthquakes of the Altai–Sayan region. *Razvedka i Okhrana Nedr* 3, 13–20.
- Brown, G.C., Mussett, A.E., 1981. *The Inaccessible Earth*. Allen and Unwin, London.
- Buslov, M.M., Geng, H., Travin, A.V., Otgonbaatar, D., Kulikova, A.V., Chen, M., Stijn, G., Semakov, N.N., Rubanova, E.S., Abildad-
- va, M.A., Voitishchek, E.E., Trofimova, D.A., 2013. Tectonics and geodynamics of Gorny Altai and adjacent structures of the Altai–Sayan folded area. *Russian Geology and Geophysics (Geologiya i Geofizika)* 54 (10), 1250–1271 (1600–1627).
- Council, J.L., le Mouel, J.L., Menvielle, M., 1986. Associate and conjugate directions concepts in magnetotellurics. *Annu. Geophys.* 4B (2), 115–130.
- Dobretsov, N.L., Buslov, M.M., Vasilevsky, A.N., Vetrov, E.V., Nevedrova N.N., 2016. Cenozoic history of topography in southeastern Gorny Altai: thermochronology and resistivity and gravity records. *Russian Geology and Geophysics (Geologiya i Geofizika)* 57 (11), 1525–1534 (1937–1948).
- Druskin, V.L., Knizhnerman, L.A., 1988. A spectral semi-discrete method for the numerical solutions of 3D nonstationary problems in electrical prospecting. *Fizika Zemli* 8, 63–74.
- Emanov, A.F., Emanov, A.A., Leskova, E.V., Kolesnikov, Yu.I., Yankaitis, V.V., Filina, A.G., 2012. The $M_s = 7.0$ Uureg Nuur earthquake of 15.05.1970 (Mongolian Altai): the aftershock process and current seismicity in the epicentral area. *Russian Geology and Geophysics (Geologiya i Geofizika)* 53 (10), 1090–1099 (1417–1431).
- Ivanov, P.V., Pushkarev, P.Yu., Three-Dimensional Inversion of the Single-Profile Magnetotelluric Data. *Izvestiya. Phys. Solid Earth* 48 (11–12), 871–876.
- Jones, A.G., 1988. Static shift of magnetotelluric data and its removal in a sedimentary basin environment. *Geophysics* 53, 967–978.
- Kissin, I.G., 2009. *Crustal Fluids: Geophysical and Tectonic Aspects* [in Russian]. Nauka, Moscow.
- Kiyani, D., Jones, A.G., Vozar, J., 2014. The inability of magnetotelluric off-diagonal impedance tensor elements to sense oblique conductors in three-dimensional inversion. *Geophys. J. Int.* 196, 1351–1364.
- Kuznetsova, K.I., Lukina, N.V., Kuchai, O.A., 1999. Crustal and upper mantle deformation: Cause-and-effect relationships (Altai–Sayan region). *J. Volcanol. Seismol.* 4–5, 41–49.
- Liseikin, A.V., Soloviev, V.M., 2005. The epicentral area of the Chuya earthquake (Gorny Altai): three-dimensional velocity structure. *Russian Geology and Geophysics (Geologiya i Geofizika)* 46 (10), 1061–1070 (1073–1082).
- Matrosov, P.S., Shaposhnikova, G.N., (Eds.), 1988. Altai–Sayan and Transbaikalia–Upper Amur regions, in: *Geological Structure of the USSR and Regularities in Distribution of Mineral Resources, Vol. 7* [in Russian]. Nedra, Leningrad.
- Miensopust, M.P., Queralt, P., Jones, A.G., 2013. Magnetotelluric 3D inversion—review of two successful workshops on forward and inversion code testing and comparison and the 3D MT modelers. *Geophys. J. Int.* 193, 1216–1238.
- Novikov, I.S., 2004. *Morphotectonics of Altai* [in Russian]. Geo, Novosibirsk.
- Rebetsky, Yu.L., Kuchai, O.A., Marinin, A.V., 2013. Stress state and deformation of the Earth's crust in the Altai–Sayan mountain region. *Russian Geology and Geophysics (Geologiya i Geofizika)* 54 (2), 206–222 (271–291).
- Rice, J.R., 1982. *Earthquake Focal Mechanism* [in Russian]. Mir, Moscow.
- Rodkin, M.V., Rundquist, D.V., 2017. *Geofluid Geodynamics: Applications in Seismology, Tectonics, and Ore and Petroleum Genesis* [in Russian]. Intellect, Dolgoprudnyi.
- Siripunvaraporn, W., Egbert, G., Lenbury, Y., Uyeshima, M., 2005. Three-dimensional magnetotelluric inversion: data-space method. *Phys. Earth Planet. Int.* 150, 3–14.
- Van'yan, L.L., 1997. *Electromagnetic Sounding* [in Russian]. Nauchnyi Mir, Moscow.